J. Fluid Mech. (1987), *vol.* 177, *pp.* 307–337
Printed in Gr tain

The motion of a cylinder of fluid released from rest in a cross-flow

By JAMES W. ROTTMAN†, JOHN E. SIMPSON
Department of Applied Mathematics and Theoretical Physics, University of Cambridge,
Silver Street, Cambridge CB3 9EW, UK

AND PETER K. STANSBY
Department of Engineering, Simon Engineering Laboratories, University of Manchester,
Oxford Road, Manchester M13 9PL, UK

(Received 19 June 1985 and in revised form 18 September 1986)

The two-dimensional motion of a cylinder of fluid released from rest into a flow that is uniform far upstream of the cylinder is studied. We consider cases where the cylinder is initially of circular cross-section and the fluid is either inviscid or viscous. For the inviscid fluid, we use analytical methods to determine the motion for small and large times after release and three numerical methods, the vortex-sheet method, the vortex-blob method and the vortex-in-cell method, to determine the intermediate-time motion. For the viscous-fluid problem we use the vortex-in-cell method with random walks to compute both the initial flow around the cylinder and the motion of the released fluid at a Reynolds number of 484. In the inviscid case, the released fluid deforms into a structure that resembles a vortex pair that propagates downstream at a speed less than the onset flow speed. In the viscous case, after a wake representative of a Kármán vortex street has developed, the released fluid usually deforms into an elongated horseshoe shape that travels downstream at a speed greater or less than the incident flow speed (depending on when in the vortex-shedding cycle the cylinder is released). The results of the numerical calculations are compared with some simple experiments in a water channel.

1. Introduction

This paper describes a study of how a volume of fluid released from rest in a surrounding flow is subsequently deformed and accelerated. Although there are several ways that such a flow may be produced in practice, the specific application we had in mind was the series of field trials carried out recently at Thorney Island, UK, as part of the UK Health & Safety Executive's research programme on the atmospheric dispersion of heavy gases, McQuaid (1984). In these trials a cylinder of gas was released into the atmosphere by rapidly pulling the sides of its containment vessel (made of plastic sheeting) to the ground with the assistance of elastic cords. This method was successful in producing an unconfined cylinder of gas momentarily at rest in the ambient flow. Similar release methods have been used in the field experiments described by Picknett (1981) and in the wind-tunnel simulations described by Hall, Hollis & Ishaq (1984).

---

† Present address: Department of Marine, Earth & Atmospheric Sciences, North Carolina State University, Raleigh, NC 27695, USA.

For simplicity we consider only two-dimensional flows of incompressible fluids. Specifically, we take the cross-section of the cylinder containing the fluid at rest to be circular and we calculate the subsequent motion of the released fluid. First we consider the case for which the two fluids are inviscid and the initial conditions are those of steady potential flow about the cylinder. In the second case the two fluids are viscous and before release we have either a uniformly accelerating flow of short duration or a flow with constant velocity of long duration incident on the cylinder. After release the onset velocity is always constant and the Reynolds number (based on the diameter of the cylinder) is 484. In this latter case, the initial flows about the cylinder must be computed numerically, as must the subsequent motion after the cylinder wall is removed. The methods we use are mostly numerical, but we are able to use some analytical techniques for small- and large-time motion in the inviscid-flow case.

We use the so-called vortex-sheet method (descriptions of the various vortex methods for computing fluid flows are given, for example, in review articles by Saffman & Baker 1979 and Leonard 1980) to compute numerically the initial motion for the inviscid-flow problem. When both fluids are inviscid, the total flow is represented by an infinitesimally thin vortex sheet that separates the released fluid from the surrounding fluid. The numerical method computes the motion of this vortex sheet. We found that the vortex-sheet method breaks down a short time after the contained fluid is released, a well-known difficulty with this method. As discussed more fully by Moore (1979, 1981), vortex sheets that are not being rapidly stretched everywhere are susceptible to Helmholtz instability which results, in finite time, in the development of a singularity in the sheet. We use a filtering technique proposed by Krasny (1986*a*) in the vortex-sheet method to accurately compute the motion up to the time the singularity appears. The questions of existence and uniqueness of solutions for the strictly inviscid problem after the appearance of the singularity have not been fully resolved and apparently the vortex-sheet method is not convergent after this time.

In real flows this instability is inhibited by slight thickening of the vortex sheet due to viscous diffusion. We use two numerical methods, the vortex-blob method (a modification of the vortex-sheet method) and the vortex-in-cell method, to mimic this thickening in a somewhat *ad hoc* way. Both methods, in effect, replace the infinitesimally thin vortex sheet with one of finite thickness. The vortex-in-cell method (at least of the form used here) causes a sheet to break up into fine-scale structures but experience, e.g. Baker (1979), suggests that large-scale features are not significantly affected and for our problem the general features of the results using these two methods are in quite good agreement. These methods stabilize the calculation, permitting us to compute the motion for times after the singularity appears in the strictly inviscid flow, although the problem has to be slightly redefined (since it is no longer strictly inviscid) to allow this.

For the viscous problem we use the fractional step method of Chorin (1973) to solve the 'vorticity equation' by splitting it into its convective and diffusive parts. The convective part is solved by time-stepping the positions of point (or discrete) vortices in an inviscid calculation and diffusion is superimposed by adding normally distributed random walks to the orthogonal coordinates of each vortex at each time-step. A large number of discrete vortices is required to give satisfactory flow simulations and they are handled efficiently in the inviscid part of the calculation by the vortex-in-cell method, which is well suited to fields of vorticity, e.g. Christiansen (1973). (The vortex-in-cell method for sheets has the same formulation since the sheet is represented as a series of point vortices). The no-slip condition at a solid boundary is satisfied at each time-step by introducing a vortex sheet at the surface, which then diffuses into the flow as discrete vortices. This formulation has previously been applied to flow around cylinders by Stansby & Dixon (1983) and to oscillatory flows over plane and wavy beds by Smith & Stansby (1985). Here we use the method with steady incident flow to generate a wake representative of a Kármán vortex street before release. We also use uniformly accelerating incident flows of various short durations before release (after which the incident flow is steady) to create physically possible, though somewhat artificial, situations to compare with the 'stabilized' inviscid calculations mentioned above. In both cases there will be a thin layer of vorticity on the cylinder surface.

The results of the calculations show that the circular cross-section of the released fluid first deforms, in all cases, by lengthening in the cross-stream direction and shortening in the streamwise direction. In the inviscid or 'thin-layer' case, the released fluid then quickly evolves into a structure that resembles a vortex pair propagating downstream at a speed somewhat less than the speed of the surrounding flow. In the viscous case with a well-developed wake, the released fluid generally evolves into an irregular, elongated horseshoe shape that travels downstream with a speed greater or less than that of the surrounding flow, depending on when in the vortex-shedding cycle the fluid is released.

We also report the results of some simple experiments in a water channel, which consist of the release of dyed, neutrally buoyant fluid in a continuous-flow channel. The visual results are in modest qualitative agreement with the calculations. For the case with a well-developed wake we measured the position of the centre of mass of the released fluid as a function of time and found that it compares favourably with the computed values.

The inviscid-fluid problem is discussed in §2. After the mathematical formulation of the problem, some analysis of the very small-time behaviour is described, then the results of the numerical calculations are presented and finally some analysis of the large-time behaviour is given. The case with a well-developed wake is discussed and the results of the numerical calculations are presented in §3. The experimental techniques and results are described in §4. In the appendices we outline the three numerical techniques.

2. Release with inviscid fluids

We first consider the problem for inviscid fluids. Initially a cylinder of fluid with a circular cross-section of radius r_0, is at rest in a surrounding potential flow of fluid of possibly different density. The surrounding flow far from the cylinder is uniform with speed U_0. At time $t = 0$ the cylinder wall is dissolved instantaneously, releasing the fluid contained inside into the surrounding flow. Since the fluids are inviscid, the vortex sheet that marks the boundary between the surrounding fluid and the fluid originally contained in the cylinder is convected with the fluid flow and does not diffuse. A sketch of this boundary, denoted by $S(t)$ at some time after the cylinder wall is dissolved, is shown in figure 1, which serves to define the coordinate system and nomenclature used in the later sections of this paper.

2.1. *Problem formulation*

Quantities associated with the released fluid will be denoted by a subscript 1 and those associated with surrounding fluid by a subscript 2. Since the flow is irrotational inside

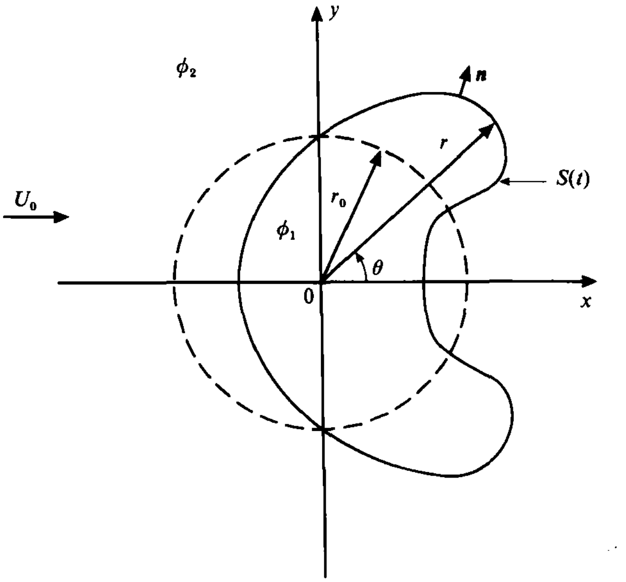

FIGURE 1. A definition sketch of the flow. The dashed line represents the initial boundary of contained fluid. The solid line represents this boundary at some time after release.

and outside $S(t)$, we can define in the conventional way a velocity potential ϕ in each of these two regions. Since both fluids are incompressible, the velocity potentials satisfy the field equations

$$\nabla^2\phi_1 = 0 \tag{2.1}$$

$$\nabla^2\phi_2 = 0. \tag{2.2}$$

The boundary conditions are that the fluid velocities normal to $S(t)$ are continuous,

$$\frac{\partial\phi_1}{\partial n} = \frac{\partial\phi_2}{\partial n} \quad \text{on } S(t), \tag{2.3}$$

where n is a coordinate measuring distance normal to the interface, that the pressure is continuous across $S(t)$,

$$p_1 = p_2 \quad \text{on } S(t), \tag{2.4}$$

and that the surrounding flow is uniform with speed U_0 far from the cylinder,

$$\frac{\partial\phi_2}{\partial x} \rightarrow U_0 \quad \text{as } r \rightarrow \infty. \tag{2.5}$$

The pressure can be eliminated from the problem by use of Bernoulli's theorem, which in the two regions may be expressed as

$$p_1 + \rho_1\frac{\partial\phi_1}{\partial t} + \tfrac{1}{2}\rho_1(\nabla\phi_1)^2 = 0, \tag{2.6}$$

$$p_2 + \rho_2\frac{\partial\phi_2}{\partial t} + \tfrac{1}{2}\rho_2(\nabla\phi_2)^2 = 0. \tag{2.7}$$

Using (2.6) and (2.7) in (2.4) gives the new boundary condition,

$$\frac{\partial}{\partial t}\left(\phi_1 - \frac{\rho_2}{\rho_1}\phi_2\right) + \frac{1}{2}\left[(\nabla\phi_1)^2 - \frac{\rho_2}{\rho_1}(\nabla\phi_2)^2\right] = 0 \quad \text{on } S(t). \tag{2.8}$$

Note that we consider only inertial effects due to the different densities of the two fluids, so the acceleration of gravity does not appear in (2.6)–(2.8).

The initial conditions are

$$X(\theta_0, 0) = r_0 \cos\theta_0, \quad Y(\theta_0, 0) = r_0 \sin\theta_0, \tag{2.9a, b}$$

$$\phi_1(r, \theta, 0) = 0, \quad \phi_2(r, \theta, 0) = U_0\left(r + \frac{r_0^2}{r}\right)\cos\theta, \tag{2.10a, b}$$

where $X(\theta_0, t)$ and $Y(\theta_0, t)$ are the coordinates of a parametric representation of $S(t)$ in terms of the parameter θ_0 (the initial angular positions of fluid particles marking the interface).

The problem then, is to determine ϕ_1, ϕ_2 and the position of the interface $S(t)$ at subsequent times. The vortex-sheet method, which solves numerically the problem outlined here, is outlined in Appendix A.

2.2. *Very small time*

Before the cylinder wall is removed, the flow is steady and exerts no net force on the cylinder. A natural question that arises at this point is how does an unsteady flow develop and how does this produce a net force on the contained fluid when it is released. The answer is that after the cylinder wall is removed, the first change that occurs is an instantaneous (since both fluids are incompressible) adjustment of the pressure field such that the pressure which was originally discontinuous across $S(t)$ becomes continuous. This adjustment of the pressure field in both regions of the flow, inside and outside $S(t)$, causes the resulting unsteady motion and leads to the development of a net force, as we shall show.

We can compute the adjustment to the pressure field from the conservation equations for mass and momentum. Let the pressure in the two fluids at the instant the wall is removed be represented as

$$p_1 = p_1^{(-)} + p_1^{(+)}, \tag{2.11}$$

$$p_2 = p_2^{(-)} + p_2^{(+)}, \tag{2.12}$$

where $p_1^{(-)}$, $p_2^{(-)}$ satisfy the steady momentum equations before the wall is removed and $p_1^{(+)}$, $p_2^{(+)}$ are the adjustments to the pressure field at the instant the wall is removed. From (2.6), (2.7), (2.9) and (2.10), we obtain

$$\frac{p_1^{(-)}}{\frac{1}{2}\rho_2 U_0^2} = C_1, \tag{2.13}$$

$$\frac{p_2^{(-)}}{\frac{1}{2}\rho_2 U_0^2} = 2\frac{r_0^2}{r^2}\cos 2\theta - \frac{r_0^4}{r^4} + C_2, \tag{2.14}$$

where C_1 and C_2 are constants. Since the velocity field is unchanged at $t = 0$, the momentum equations become

$$\frac{\partial}{\partial t}(\nabla\phi_1) = -\frac{1}{\rho_1}\nabla p_1^{(+)}, \tag{2.15}$$

$$\frac{\partial}{\partial t}(\nabla\phi_2) = -\frac{1}{\rho_2}\nabla p_2^{(+)}, \tag{2.16}$$

and taking the divergence of these equations gives, with (2.1) and (2.2),

$$\nabla^2 p_1^{(+)} = 0, \tag{2.17}$$

$$\nabla^2 p_2^{(+)} = 0. \tag{2.18}$$

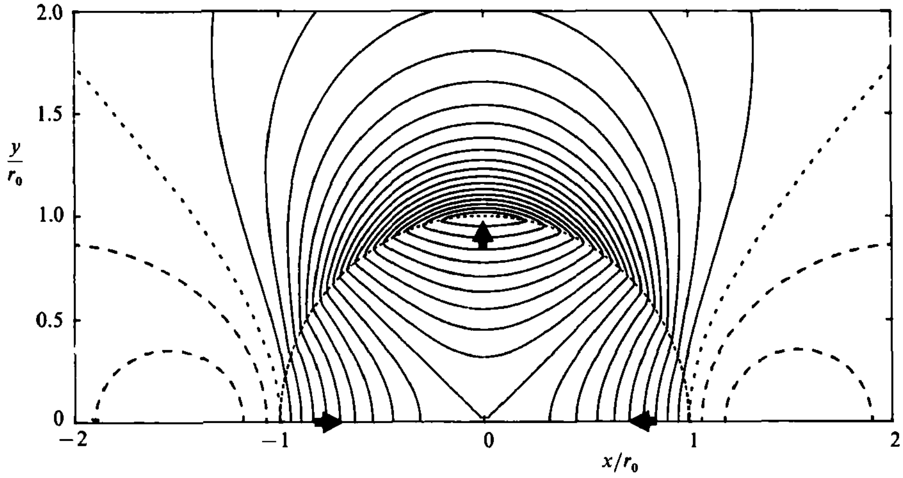

FIGURE 2. Contour plot of the pressure field just after release. The dotted contour represents an intermediate value of the pressure, the dashed contours higher values and the solid contours lower values. The arrows indicate the directions of negative pressure gradients, showing how the circular cylinder of released fluid will initially deform. Only the upper half of the plot is shown since the flow is symmetric about the x-axis.

The boundary conditions are

$$p_1^{(-)}+p_2^{(+)} = p_2^{(-)}+p_2^{(+)} \quad \text{on } r = r_0, \tag{2.19}$$

$$\frac{\partial p_1^{(+)}}{\partial r} = \frac{\partial p_2^{(+)}}{\partial r} \quad \text{on } r = r_0, \tag{2.20}$$

and

$$p_2^{(+)} \rightarrow 0 \quad \text{as } r \rightarrow \infty. \tag{2.21}$$

Boundary condition (2.20) ensures that the component of velocity normal to the surface $r = r_0$ remains continuous across this interface. The solution of this problem is

$$\frac{p_1^{(+)}}{\frac{1}{2}\rho_2 U_0^2} = 2\left(1+\frac{\rho_2}{\rho_1}\right)^{-1}\frac{r^2}{r_0^2}\cos 2\theta - 1 + C_2 - C_1, \tag{2.22}$$

$$\frac{p_2^{(+)}}{\frac{1}{2}\rho_2 U_0^2} = -2\frac{\rho_2}{\rho_1}\left(1+\frac{\rho_2}{\rho_1}\right)^{-1}\frac{r_0^2}{r^2}\cos 2\theta. \tag{2.23}$$

A contour plot of the pressure fields p_1 and p_2 is shown in figure 2. From (2.15) and (2.16), which are valid for small times, it is clear that the initial perturbations to the steady velocity field are due to gradients of the adjustments to the pressure field. The contour plot in figure 2 indicates that the perturbed motion is such that the circle will elongate in the cross-stream direction and shorten in the streamwise direction, as indicated by arrows in the plot (representing negative pressure gradients).

The vortex-sheet method assumes this continuous pressure distribution automatically and is more efficient for computing the subsequent motion than continuing with the above procedure. We can determine the initial motion of the interface formally by developing a perturbation solution of the vortex-sheet equations. Expanding all dependent variables in Taylor series in non-dimensional time $\tau = tU_0/r_0$, substituting these series into (A 3)–(A 8), and equating terms of equal order in τ up to $O(\tau^3)$, we obtain the following expressions for the parametric representation of $S(t)$:

$$X(\theta_0, \tau) = \tfrac{2}{3}\kappa^2 r_0 \tau^3 + (1-\kappa\tau^2)\, r_0 \cos\theta_0 - 2\kappa^2\tau^3 r_0 \cos 2\theta_0 + O(\tau^4), \qquad (2.24)$$

$$Y(\theta_0, \tau) = (1+\kappa\tau^2)\, r_0 \sin\theta_0 + 2\kappa^2\tau^3 r_0 \sin 2\theta_0 + O(\tau^4), \qquad (2.25)$$

where $\kappa = (\rho_2/\rho_1)/(1+\rho_2/\rho_1)$. It is clear from these expressions that the interface does not move at all up to $O(\tau)$. At $O(\tau^2)$ the interface deforms into an ellipse with its minor axis, which decreases with time, along the streamwise direction and its major axis, which increases with time, perpendicular to the streamwise direction. Up to this order the flow remains symmetrical upstream and downstream of the plane through the origin and perpendicular to the mean flow direction and there is no net force on the released fluid. However, the flow is no longer steady and at $O(\tau^3)$ an asymmetric flow develops owing to the nonlinear interaction of the motion of the released fluid with the surrounding flow. Plots of the interface shape described by (2.24) and (2.25) are shown in figure 3 for a few values of κ and τ.

A consequence of this asymmetric flow is that a net force is imposed on the released fluid. The force is along the direction of the mean flow. In fact, the position of the centre of mass of the released fluid is given by

$$\overline{X}(\tau) = \tfrac{2}{3}\kappa^2 r_0 \tau^3 + O(\tau^4), \quad \overline{Y}(\tau) = 0. \qquad (2.26)$$

Higher-order terms in the power-series expansion can be calculated to determine the motion for larger times after release, but this soon becomes very tedious. Instead, we chose to use a numerical method to compute directly the evolving shape of the interface.

2.3. *Small time*

The accurate numerical solution of problems of the type that we have posed here has proved in the past to be rather difficult. Indeed, Baker (1980) attempted to solve our problem for the case when $\rho_2/\rho_1 = 1$ using an improved version of the vortex-sheet method of Fink & Soh (1978) and found that the results of his numerical calculations were unreliable; the sheet crossed itself at some time after the initiation of the motion and this time became smaller as the number of points representing the interface was increased (when the calculation should have been becoming more accurate). Baker was unable to give any definitive reasons for the breakdown of his calculations, but he pointed out that there are several unresolved questions about the fundamental nature of vortex sheets and their suitability to numerical solution.

The work of Moore (1979), Meiron, Baker & Orszag (1982), and Krasny (1986*a*) suggests that flat uniform vortex sheets that are given sinusoidal perturbations develop a singularity at some finite time. At this time, the vortex sheet is generally smooth and only slightly distorted from its initial state but its curvature has become singular and the vorticity distribution has developed a cusp at some point. This singularity is apparently the result of nonlinearity and Helmholtz instability. Nonlinearity spreads an initial disturbance throughout the spectrum and then Helmholtz instability, in which the growth rate of disturbances is proportional to their wavenumber, makes the small wavelengths grow so fast that at a critical time, which is a function of the initial conditions, the analyticity of the solution is destroyed. The evidence indicates that a unique solution exists up to this critical time. Similar results were found by Schwartz (1981) in an investigation of vortex sheets of finite length and non-uniform vorticity distributions. Moore (1981) suggests that

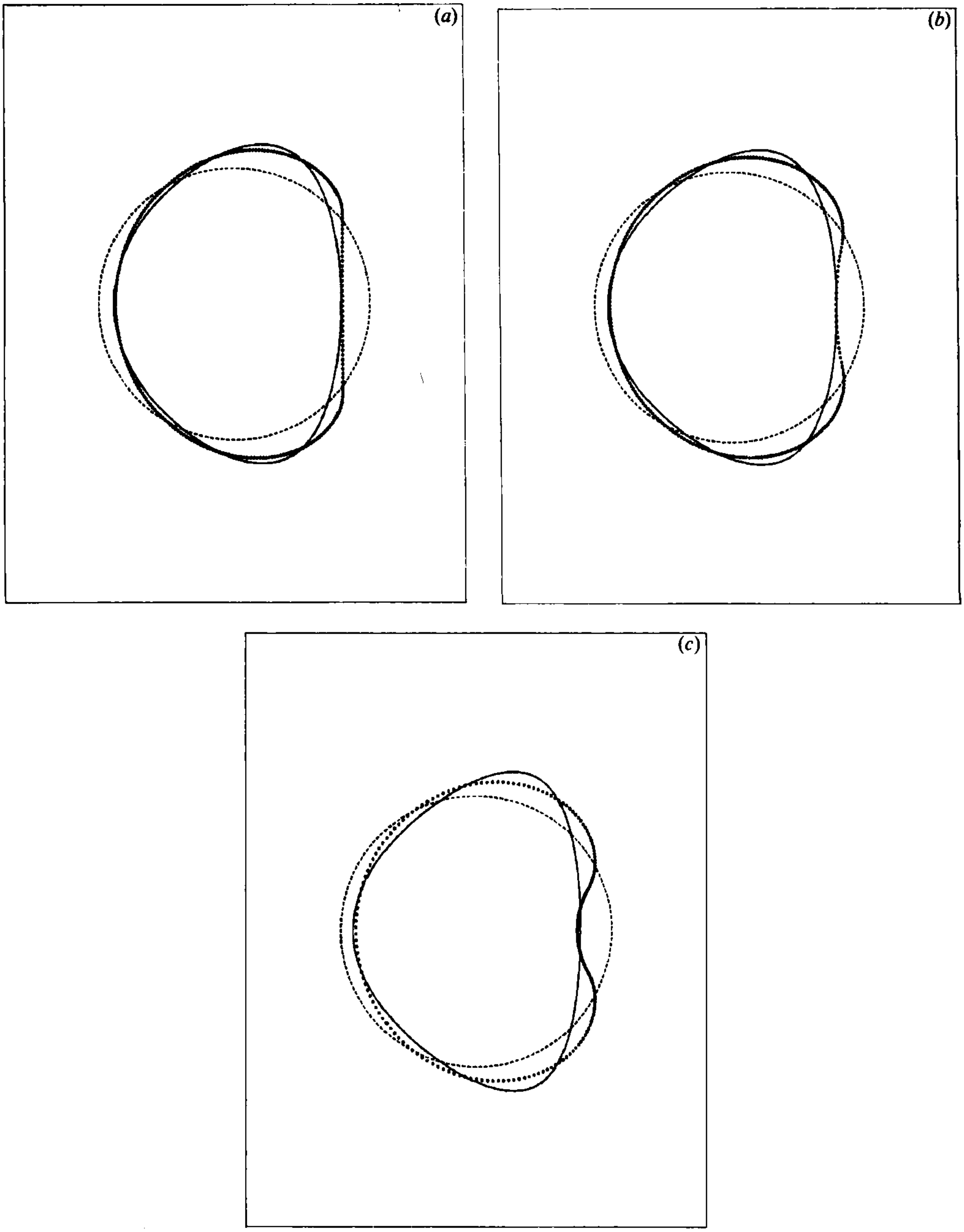

FIGURE 3. The interface shape near the critical time at which the vortex sheet becomes singular; ----, $\tau = 0$; ······, computed shape using 256 markers; ——, third-order Taylor series (2.24) and (2.25). (*a*) $\rho_2/\rho_1 = 0.5$, $\tau = 0.70$, (*b*) $\rho_2/\rho_1 = 1.0$, $\tau = 0.55$, (*c*) $\rho_2/\rho_1 = 2.0$, $\tau = 0.49$.

a singularity can develop in all vortex sheets that are not being sufficiently rapidly stretched everywhere.

It is not surprising that numerical methods do not converge for times after the appearance of the singularity. However, Krasny (1986*a*) argues that most numerical methods are also not convergent even for times before the critical time. The failure of a vortex-sheet method to converge to a unique solution before the critical time, according to Krasny, is due to the use of finite-precision arithmetic. Round-off error introduces spurious perturbations into the solution and once introduced these perturbations grow according to the dynamics of the equations. The larger the number of points used to represent the vortex sheet in the calculations, the higher the wavenumber at which spurious disturbances are introduced and, as a consequence of Helmholtz instability, the sooner the singularity appears. Smoothing techniques of the type that is inherent in Fink & Soh's method can slow down the effects of Helmholtz instability but these techniques do not make vortex-sheet methods convergent and they introduce errors into the calculation at all wavelengths.

Krasny (1986*a*) proposes a filtering technique that inhibits the destructive effects of round-off error and minimizes inaccuracies introduced by smoothing the solution. This technique does not prevent the growth of the small-wavelength motions that evolve from nonlinear interactions, but it does suppress any motion initially introduced by round-off error. Specifically, the filtering technique consists of taking fast Fourier transforms of the solution at each time-step and setting to zero the amplitudes that have magnitudes less than the floating-point precision of the calculation. This means that a Fourier coefficient must increase in magnitude greater than the floating-point precision in one time-step to get through the filter. Once all the coefficients have magnitudes greater than this precision, the filter has no further effect. Krasny (1986*a*) applied this technique to the problem of a periodically perturbed flat vortex sheet and was able to obtain convergent results up to the estimated time that the curvature singularity appears.

We have attempted to use Krasny's filtering procedure with a vortex-sheet method to estimate the critical time τ_c for the problem we have outlined here. The particular numerical implementation of the vortex-sheet method that we used is adapted from Roberts (1983). Our implementation of Krasny's procedure is slightly different from his in that we filter the time derivative of the solution as opposed to the solution itself. The primary reason for this change is that it is more convenient with our time integration scheme. The effects of the filter should be unaltered. The details of the numerical method are given in Appendix A. Here we describe the results of the calculations.

Calculations were done for three density ratios: $\rho_2/\rho_1 = \frac{1}{2}$, 1 and 2. The calculations were performed in double precision (about 14 decimal digits) and the filter threshold was set at 10^{-13}. In each case we observed that the calculation developed a sawtooth instability at a time that decreased as the number of points N representing the interface increased. However, this time seemed to be converging to some non-zero value. We also monitored the time at which the filter became no longer effective; that is, the time when first all Fourier amplitudes were larger than 10^{-13}. This time increased as the number of points increased and seemed to be converging to the time when the instability first appeared. Table 1 lists these filter cut-off times τ_c as a function of the number of points used to describe the interface. Also listed in this table are extrapolated values for these cut-off times τ_c^∞ corresponding to $N = \infty$. These were obtained by assuming that

$$\tau_c \sim \tau_c^\infty + \frac{a_1}{N},$$

as $N \rightarrow \infty$ and determining τ_c^∞ and a_1 by a least-squares fit to the computed values of τ_c. The correlation coefficients, also shown in the table, indicate that the data fits this relationship very well. For the largest number of points (512 for $\rho_2/\rho_1 = 1$ and

	τ_c		
N	$\rho_2/\rho_1 = 0.5$	$\rho_2/\rho_1 = 1.0$	$\rho_2/\rho_1 = 2.0$
32	0.268	0.192	0.170
64	0.460	0.333	0.353
128	0.585	0.465	0.444
256	0.653	0.520	0.471
512	—	0.521	—
⋮	⋮	⋮	⋮
∞	0.695 $(r = -0.997)$	0.549 $(r = -0.991)$	0.524 $(r = -0.999)$

TABLE 1. The critical time τ_c at which the filter is no longer effective with a threshold of 10^{-13} in the strictly inviscid calculations as a function of the number of points N used to describe the interface. The values corresponding to $N = \infty$ were obtained by assuming a linear relationship between τ_c and $1/N$ whose coefficients are determined by a least-squares fit to the computed values of τ_c. The correlation coefficient r for the least-squares fit is shown in parenthesis.

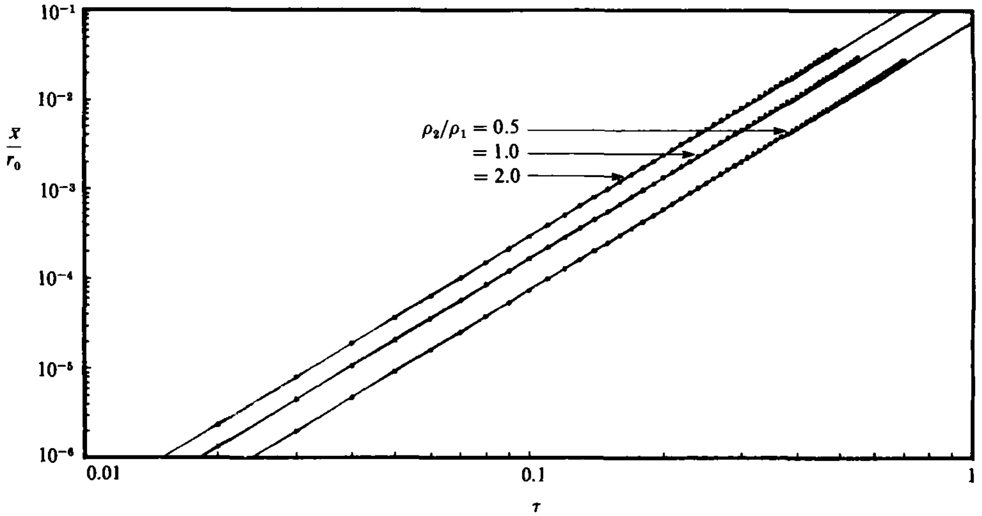

FIGURE 4. A plot of the centroid position $\bar{X}$ as a function of time after release for the three density ratios $\rho_2/\rho_1 = 0.5, 1.0, 2.0$: •, as computed using the vortex sheet method with 256 markers; ——, third-order Taylor series (2.26).

256 for $\rho_2/\rho_1 \neq 1$) the calculation broke down very soon after the filter cut-off time, so we propose that these extrapolations are estimates of the times when a singularity of some sort appears. These times are $\tau_c^\infty = 0.70$, 0.55 and 0.52 respectively, for the density ratios given above.

Figure 3 shows the shape of the vortex sheet near τ_c^∞ for the three density ratios. The numerically computed shapes are represented by the solid circles, which are at the actual positions of the marker particles, for the case with 256 particles. Using a larger number of points does not change the profile shape within the accuracy of the graph. The third-order Taylor-series solution (2.24) and (2.25) is represented by the solid line. As can be seen the profiles are smooth and only slightly distorted from their initially circular shapes. In fact, the Taylor-series solutions are quite close to

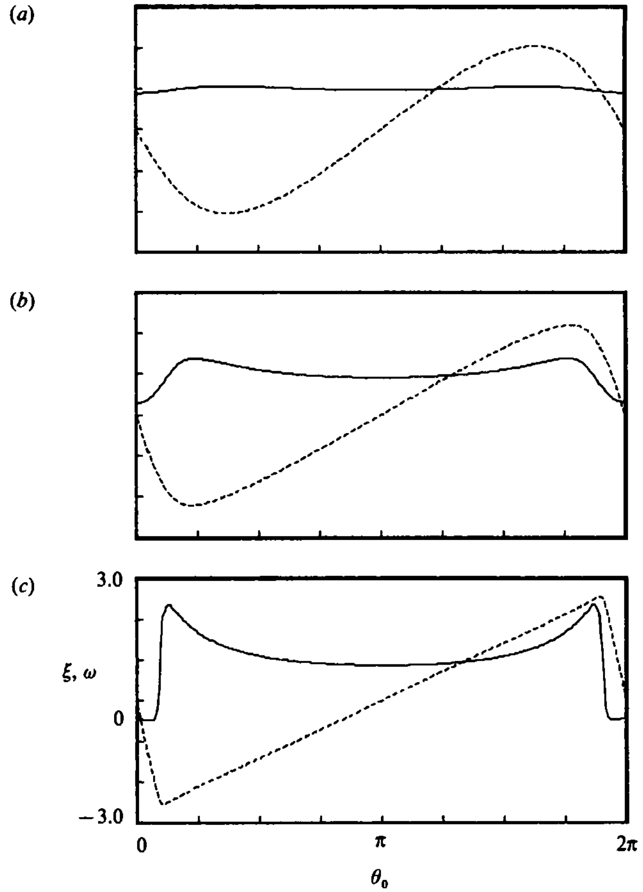

FIGURE 5. Plots of the vortex-sheet curvature ξ and vorticity strength per unit arclength ω as functions of the parameter θ_0 at several times after release for the case with $\rho_2/\rho_1 = 1.0$: ——, ξ; ----, ω.

the numerical solutions. Figure 4 is a plot of the position of the centre of mass of the released fluid as a function of the time after release and shows that the Taylor-series solution (2.26) is a very good approximation to the numerical results up to the critical time.

Figure 5 shows plots of the vortex-sheet curvature and the vorticity strength per unit arclength at three times after release for the case with $\rho_2/\rho_1 = 1$. The data for these plots were taken from calculations in which 256 markers were used. As the critical time is approached the numerical solutions indicate that a curvature singularity develops at two points on the interface and possibly a cusp in the vorticity strength develops at each of these points. Similar results were obtained for the cases with $\rho_2/\rho_1 \neq 1$. Although we have not made an exhaustive study of the detailed nature of these singularities, the behaviour shown in figure 5 appears consistent with earlier studies of initially flat vortex sheets.

The integral invariants of the problem, such as the area of the released fluid, the horizontal impulse and the kinetic energy were monitored throughout the calculation and found to remain constant to within the accuracy of the time-stepping scheme up to the time of the onset of the sawtooth instability.

2.4. *Intermediate time*

From the results of the previous section, it is clear that the vortex-sheet method cannot be used to continue the calculation, and indeed it is not clear that a solution exists or is unique after the critical time. In the physical problem, the singular nature of Helmholtz instability is inhibited by a slight thickening of the interface due to viscous diffusion of the vorticity. We use two approaches which have been used by others to stabilize inviscid calculations, in effect by mimicing the effect of viscosity in a somewhat artificial manner.

The first approach is a modification of the vortex-sheet method, the so-called vortex-blob method. This method uses the same description of the interface as the vortex-sheet method except that the integrals describing the induced velocities have the singular parts of their integrands removed. This means essentially that the vortex sheet has a finite thickness or the vortices representing the sheet have finite cores. It is not strictly a thickening due to viscosity since the thickening does not increase with time. There are various versions of the method, many of them described in Leonard (1980). The particular implementation that we used is that of Krasny (1986*b*) and the details of the method are outlined in Appendix B.

The second approach is the so-called vortex-in-cell method, which uses point or discrete vortices to represent the sheet. Velocity is computed by distributing vorticity on to a rectangular grid and solving a finite-difference form of the Poisson equation for the stream function which is efficiently achieved using fast Fourier transforms. The velocity of a vortex (or any other point) is then determined by interpolation. The advantage of this procedure over the vortex-blob method is its greater efficiency and hence its ability to track a large number of particles. The vortex-blob method is restricted to about a few hundred particles because of computational restraints, whereas the vortex-in-cell method is able to handle several thousand. A pseudo-viscosity is introduced into the vortex-in-cell calculations by the process of distributing the vorticity from the discrete vortices on the rectangular grid and interpolating to obtain the velocity at each point. This causes fine-scale behaviour dependent primarily upon the grid spacing but also upon the number of vortices and the time-step. The grid spacing is crudely analogous to the core size of the vortex-blob method, which will be seen to have the advantage of not suffering fine-scale behaviour. The details of the vortex-in-cell method are described further in Appendix C.

We also use the viscous formulation in an attempt to compute directly, although in a somewhat artificial way, a small thickening of the vortex sheet. This is done by uniformly accelerating the onset flow for a short duration to a constant speed and then releasing the cylinder of fluid. Since the no-slip condition on the cylinder and viscous diffusion are incorporated during this short duration, a boundary layer of finite thickness is generated and released into the flow before a wake develops. We did this for various short durations to see how sensitive the calculations are to the initial conditions.

The evolution of the interface, as computed using the vortex-blob method up to $\tau = 3$, is shown in figure 6 for the case with $\rho_2/\rho_1 = 1$. The particular implementations of these methods restrict us to this value of the density ratio, and so all the remaining calculations shown in this paper will be for this case. The prediction of the interface by the vortex-in-cell method, as shown in figure 7, is in general agreement although fine-scale structures, particularly as the sheets wrap-up, make direct comparisons difficult. At $\tau = 1$ the originally circular interface has deformed into a horseshoe-like

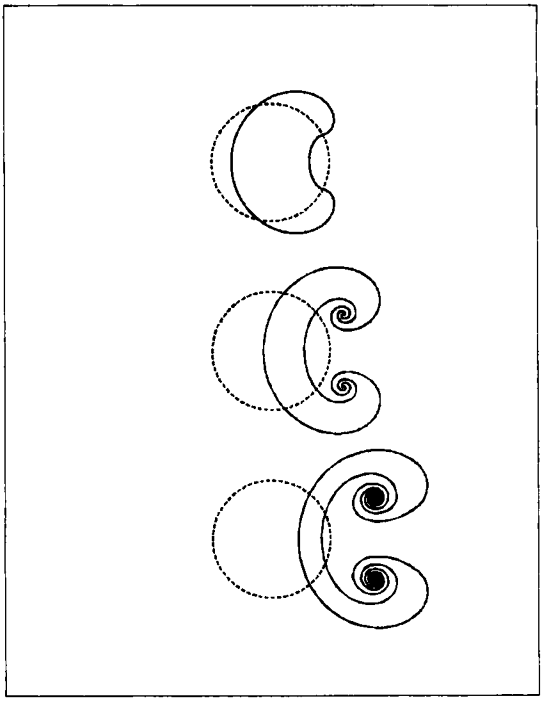

FIGURE 6. The evolution of the interface for small times after release, by the vortex-blob method, with $\delta = 0.1r_0$ and 256 vortices marking the interface at $\tau = 1.0$, 2.0, 3.0 and $\rho_2/\rho_1 = 1.0$.

shape with the open end of the shoe pointing downstream; at $\tau = 2$ the points of the horseshoe begin to wrap-up into tight spirals as the released fluid accelerates downstream, and at $\tau = 3$ the wrapping up of the released fluid into two concentrated regions of vorticity continues as the centre of mass moves further downstream. The movement of the centre of mass is essentially the same for both calculations.

We found that the smaller the core size used in the vortex-blob method, the tighter the spirals became at a fixed time and, consequently, the greater the number of marker particles required to resolve them. These results are similar to those obtained by Krasny (1986*b*) in his study of the roll-up of flat vortex sheets.

To follow the motion for larger times we used the more economical vortex-in-cell method exclusively. Vortex-particle motion and concentration contour plots up to $\tau = 8$ are shown in figure 7. It appears that the released fluid wraps up into roughly circular closed cells of fluid consisting of two contra-rotating subcells. The area of the whole cell is about three times that of the original circle. Figure 8 is a plot of the speed U_{cm} of the centre of mass of the released fluid as a function of the time after release up to time $\tau = 20$. Results with initially accelerating viscous flows of short duration τ_{s} incident on the fixed cylinder are also shown. $\tau_{\mathrm{s}} = 0$ is effectively the limiting case which is the main subject of this section. The results are quite similar. After release U_{cm} at first increases rapidly up to $\tau \approx 3$, to a value dependent on τ_{s}. As τ_{s} increases from 0 to 2, the maximum increases from $0.8U_0$ to $0.92U_0$. For $\tau \geqslant 6$, U_{cm} varies between $0.6U_0$ and $0.8U_0$ for all cases. That is, the released fluid plus the external fluid it has entrained eventually travels downstream at an approximately constant speed significantly less than U_0.

The integral invariants of the inviscid problem were monitored during the

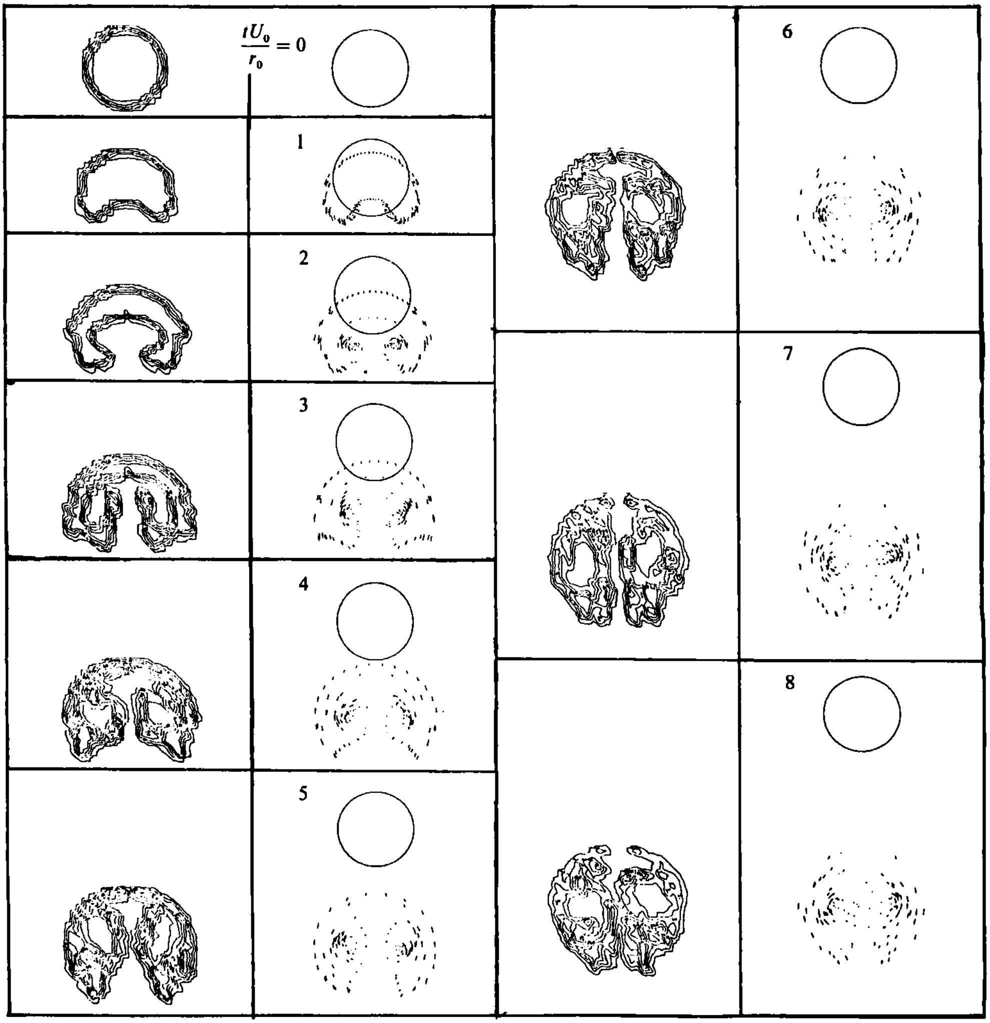

FIGURE 7. The shapes of an initially circular cylinder of fluid released from rest in a potential flow, computed using the vortex-in-cell method. The right-hand columns show the motion over one time-step ($\Delta\tau = 0.1$) of the point vortices marking the boundary of the released fluid. The left-hand column shows contours of concentration of particles marking the released fluid. Note that the free-stream flow direction in this figure is from top to bottom.

vortex-blob calculation. As would be expected, the area and horizontal impulse were conserved to within the accuracy of the numerical scheme but the energy was not. The amount of energy lost depends on the core size. The larger the core size the greater the loss of energy. For the calculations shown in figure 6 (with a core size $\delta = 0.1r_0$) the energy is about 10% less than the strictly inviscid value. The energy remains nearly constant at this lower value throughout the calculation. This is consistent with the idea that the vortex-blob method mimics an interface of fixed finite thickness. This is unlike viscosity, which continuously diffuses the vorticity in the interface (and thus continuously thickens the interface) and continuously loses energy.

It is not possible to measure the integral invariants in the vortex-in-cell calculation since fine-scale structures on the interface develop after several time-steps.

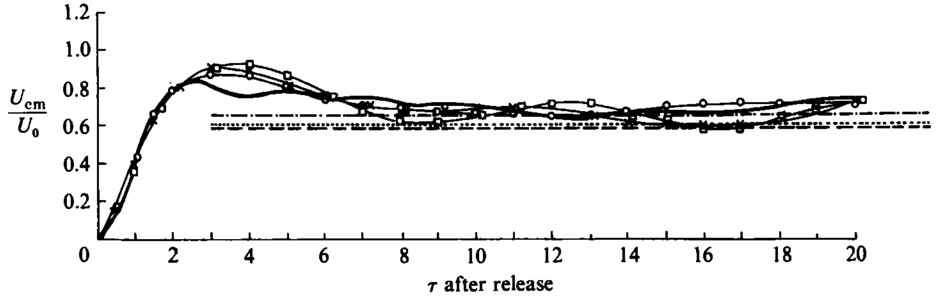

FIGURE 8. The computed speed of the centre of mass of the released fluid as a function of time after release, calculated using the vortex-in-cell method, with impulsively started inviscid flow and with viscous flow ($Re = 484$) uniformly accelerating for time τ_s before release: ——, inviscid ($\tau_s = 0$); ○, $\tau_s = 0.5$; ×, $\tau_s = 1$; □, $\tau_s = 2$. Long-time values are also shown: ……, $U_{cm} = 0.61U_0$ as given by a Pierrehumbert vortex pair; ——, $U_{cm} = 0.59U_0$ as given by a point-vortex pair; —·—·—, $U_{cm} = 0.66U_0$ as given by a non-uniform vortex pair.

2.5. *Large time*

In this section we investigate some steady-state flows that may approximate the large-time limiting solutions of the problem we are considering. The numerical calculations described in the previous section indicate that the flow eventually becomes approximately steady with respect to translating axes and the vorticity becomes confined to a translating closed cell of fluid. The vorticity is distributed antisymmetrically about the x-axis with equal magnitude on either side but opposite sign. If we neglect the possible mutual destruction of vorticity due to viscous diffusion, then the total circulation in each half-plane is conserved. Thus, the numerical calculations suggest that the flow evolves into a steady vortex pair with distributed vorticity.

Pierrehumbert (1980) describes a three-parameter family of such vortex pairs for which the vorticity is uniform within the two cores and the cores have shapes that are symmetrical about a plane perpendicular to the direction of propagation. His numerical calculations show that the family exhibits a continuous range from a pair of point vortices to a pair of vortex regions with boundaries in contact along the axis of symmetry parallel to the direction of propagation. Although it is unlikely that the vortex pair in our problem will have cores of uniform vorticity, Pierrehumbert's family of vortex pairs should be a good approximation to our limiting flow except for perhaps the size of the vortex cores.

We choose from the family of vortex pairs the one member that has the same circulation strength, fluid impulse, and energy as our inviscid flow. (We note that the analogous problem for a vortex ring has been solved by Taylor 1953 using the same criteria.) These quantities are conserved in inviscid flows with distributed vorticity as explained, for example, in Batchelor (1967). For our particular problem these quantities are, from Appendix A,

$$\Gamma_0 = 4U_0 r_0, \tag{2.27}$$

$$I_x = -\rho\pi U_0 r_0^2, \tag{2.28}$$

$$T = \pi U_0^2 r_0^2, \tag{2.29}$$

where Γ_0 is the circulation strength, I_x is the horizontal fluid impulse, and T is the total energy. To be precise, I_x and T are the impulse and energy per unit length along the x-axis. In terms of Pierrehumbert's notation, $T^* = T/\rho\Gamma_0^2 = \frac{1}{16}\pi$ is the non-dimensional energy and $X_c = I_x/\rho\Gamma_0 = \frac{1}{4}\pi r_0$ is half the distance between the centroids of vorticity.

Interpolating in Pierrehumbert's table 1, we calculate that the vortex cores are roughly elliptical in shape, not greatly distorted from a circle, with an effective radius of $0.60r_0$ and a cross-sectional area of $0.36\pi r_0^2$. The vortex pair carries with it a closed cell of fluid roughly oval in shape with a cross-sectional area of $2.51\pi r_0^2$. This implies that, in the process of wrapping up the original cylinder of fluid into the closed-cell structure, more than an equal quantity of the surrounding fluid has been entrained as well. The self-induced translation speed of the pair is $V = -0.388U_0$; that is, in a reference frame in which the fluid speed is U_0 at infinity, the closed cell of fluid travels downstream with speed $U_{\mathrm{cm}} = U_0 + V = 0.61U_0$.

It is interesting to compare these results with similar calculations assuming that the asymptotic state is a pair of point vortices or the steady flow with a non-uniform distribution of vorticity described by Batchelor (1967, pp. 534–535). Of course, in these cases we can only match the circulation strength and impulse, but since our numerical calculations are not strictly inviscid for large times, they do not conserve energy anyway and, as it turns out, the results are not greatly different. For the pair of point vortices the closed cell of fluid is nearly an ellipse with an area of $2.2\pi r_0^2$ and travels downstream with speed $U_{\mathrm{cm}} = 0.59U_0$. For the non-uniform distribution of vorticity, the closed cell of fluid is a circle with an area of $2.92\pi r_0^2$ and travels downstream with speed $U_{\mathrm{cm}} = 0.66U_0$.

From figure 7 we estimate that the cross-sectional area of the closed cell of fluid at $\tau = 8$ is between 2.8 and 3.1 times the area of the original cylinder of released fluid. The translation speeds predicted above are plotted in figure 8, along with our numerical calculations using the vortex-in-cell method. Since all three assumptions give results close to the numerical calculations, it appears that the general features of the flow at large times are fairly insensitive to the structure of the vorticity distribution.

3. Release with a well-developed wake

The basis of the numerical scheme for viscous flow has been outlined and details are given in Appendix C. We have already considered cases with a uniformly accelerating flow of short duration before release providing a thin attached layer of vorticity on the cylinder surface. In this section we consider cases with a steady flow incident on the cylinder for a sufficiently long time for boundary layers to separate and develop a wake representative of a Kármán vortex street.

3.1. *The flow before release*

The flow was initiated impulsively from rest. Previous calculations (Stansby & Dixon 1983) have shown that the wake behind the cylinder produced by the shedding of vorticity becomes periodic without imposing any kind of external asymmetry, but this requires a rather long time to be established. To reduce this time (and any errors associated with the wake reaching the downstream boundary of the computation domain) an asymmetry was artificially introduced by setting a cross-flow velocity equal to U_0 during the early stages ($0 \leqslant \tau \leqslant 1$). The resulting periodic wake flow for $Re = 484$ is shown in figure 9 at $\tau = 30$ and 32. Each small line segment represents the movement of a discrete vortex over one time-step ($\Delta\tau = 0.1$).

The time variations of drag and lift (which include the influence of surface shear

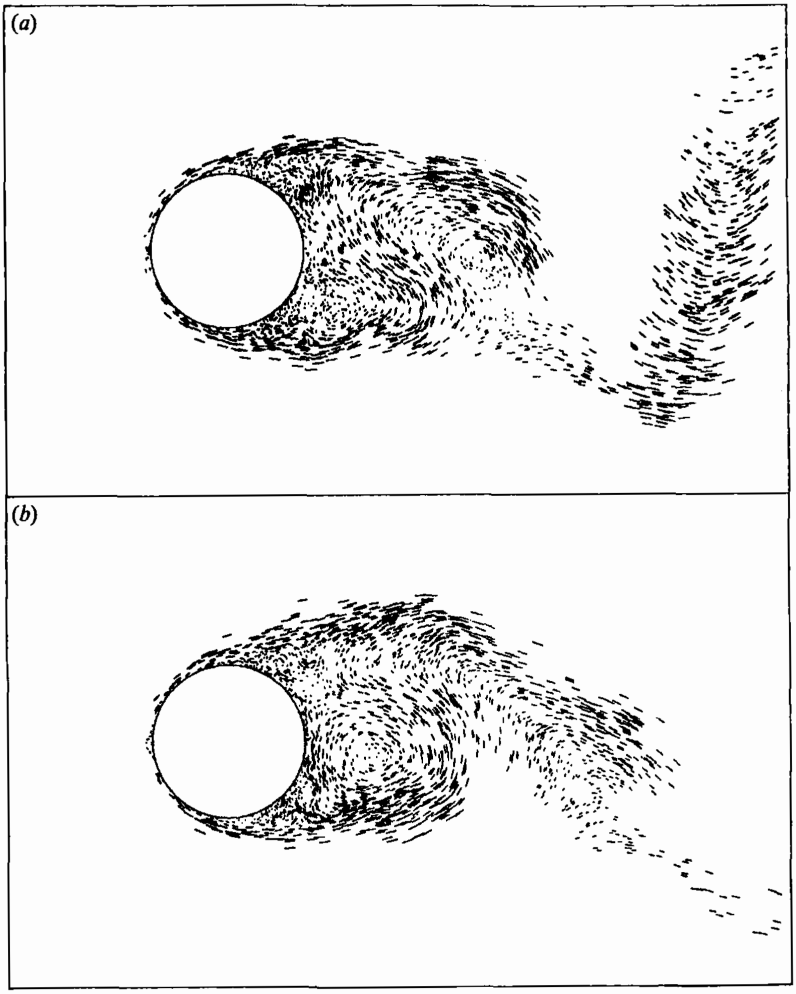

FIGURE 9. The computed vorticity structure due to steady uniform flow incident on a circular cylinder at (*a*) $\tau = 30$ and (*b*) 32, after impulsive initiation of the flow with $Re = 2U_0 r_0/\nu = 484$. The dashes show the movement of discrete vortices in one time-step ($\Delta\tau = 0.1$).

stress), non-dimensionalized by $\rho U_0^2 r_0$, are plotted in figure 10. The plots have been smoothed over five time-steps to remove a random component which is associated with the numerical method. The impulsive forces at $\tau = 0$ and 1 are caused by the impulsive changes in onset velocity. The mean non-dimensional drag is about 1.5 and the Strouhal number is very close to 0.2. The latter is in agreement with experiment while drag is overestimated by about 15%. The non-dimensional mean pressure around the cylinder (averaged between $\tau = 25$ and 50) is plotted in figure 11 (full line B). The experimental data of Thom (1928) for $Re = 250$ and 484 are also plotted. The vortex method generally underpredicts pressure, relative to the upstream stagnation pressure, around the cylinder and results computed with $Re = 250$ and 484 were virtually identical while the experiments show significant differences. For this study the vortex-in-cell method uses uniform rectangular meshes and the stream function at the cylinder surface is not exactly constant after a vortex sheet has been introduced to represent the surface at each time-step. This has been achieved by using

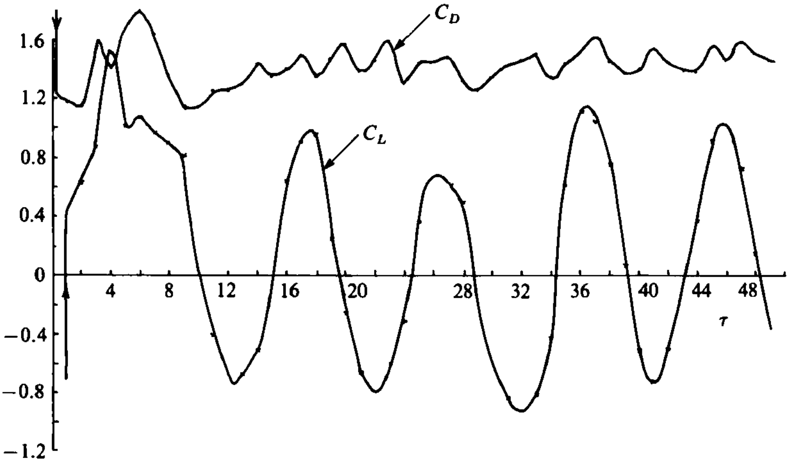

FIGURE 10. Variations of the non-dimensional drag C_D and lift forces C_L with time for the flow shown in figure 9.

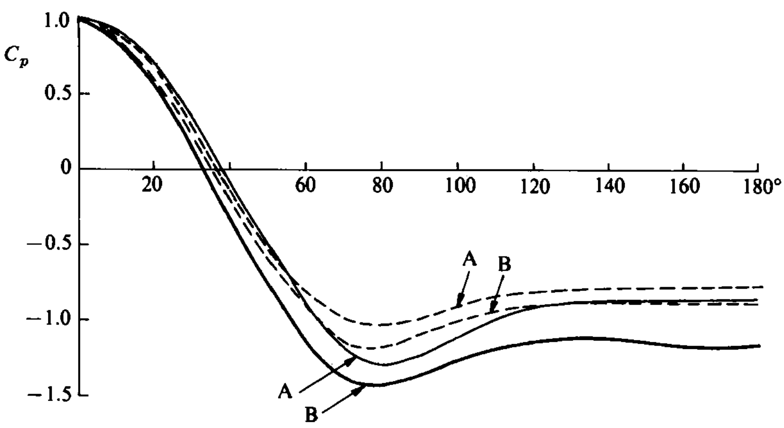

FIGURE 11. The computed non-dimensional pressure $C_p = (p-p_\infty)/\frac{1}{2}\rho U_0^2$ averaged for $25 \leqslant \tau \leqslant 50$ on the surface of the cylinder as a function of angular position is shown by the full lines: A uses a polar mesh and B uses Cartesian meshes in the vortex-in-cell method ($Re = 250$ or 484). Experimental results of Thom (1928) are shown by the dashed lines: A, $Re = 484$; B, $Re = 250$.

a polar mesh with its inner boundary coincident with the surface (Smith 1986). Results are shown in figure 11 (full line A) and agreement with experiment at $Re = 250$ is much improved. This demonstrates the sensitivity of the numerical method to the vortex-in-cell mesh and particularly to the surface boundary conditions. The polar mesh is of course inappropriate for this application where we need to calculate the motion of the enclosed fluid. However, the use of rectangular meshes may be said to approximately reproduce important features of the experimental data. Separation positions at about 93° from the front stagnation point are in reasonable agreement with experiment.

Very similar pressure distributions were produced by averaging between $\tau = 15$ and 30, suggesting that a wake representative of a long duration has become established by $\tau = 15$. Release time will in fact be varied between $\tau = 20$ and 36.

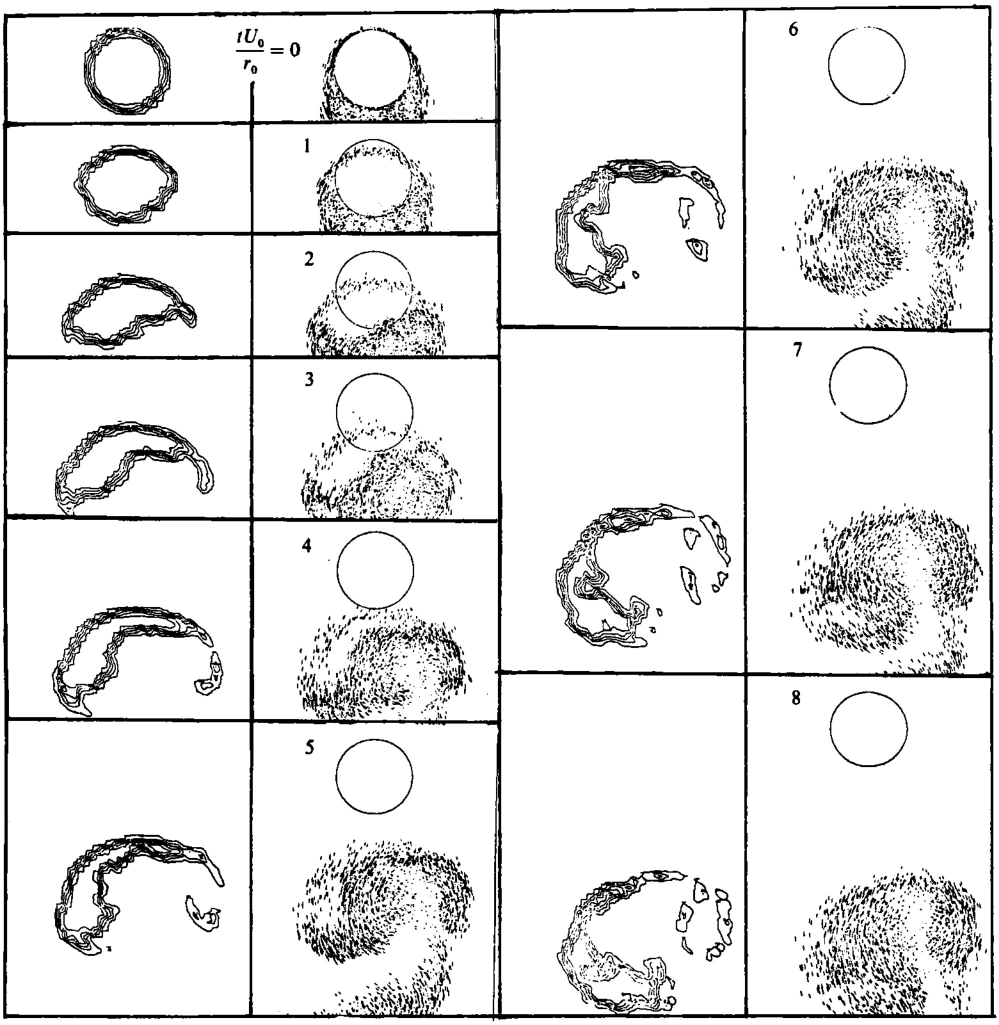

FIGURE 12. The computed shapes of an initially circular cylinder of fluid released from rest in a flow with a well-developed wake at $Re = 484$. The right-hand columns show the movement of discrete vortices in one time-step ($\Delta\tau = 0.1$). The left-hand columns show contours of concentration of particles marking the released fluid. Note that the free-stream flow direction in this figure is from top to bottom.

3.2. *The flow after release*

After the wake flow was considered to be established, the fluid inside the cylinder was released by omitting the calculation of the vortex sheet that was used to make the normal and tangential components of the fluid velocity zero at the cylinder surface. Typical resulting motion is shown in figure 12, which is analogous to figure 7. The time shown in the figure is the non-dimensional time after release.

The speed of the centre of mass of the released fluid is plotted as a function of time after release in figure 13 for various times of release. The initial behaviour is always very similar but the longer-term behaviour can be quite different. As shown in figure 12, the released fluid initially elongates in the cross-stream direction and then begins to form a rough horseshoe shape similar to the early stages of the inviscid-flow

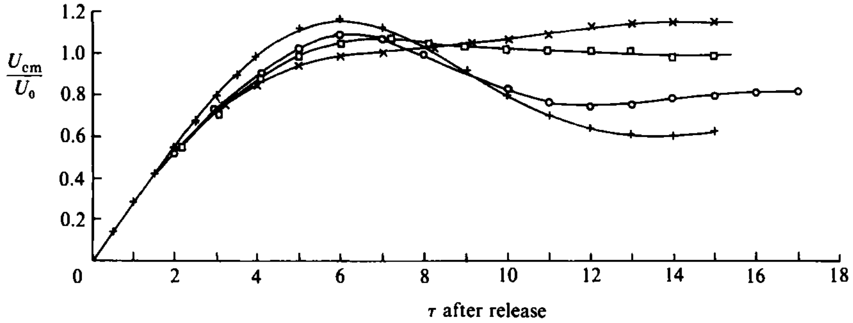

FIGURE 13. The computed speed of the centroid of the released fluid as a function of time after release, in a flow with a well-developed wake at $Re = 484$. The different curves represent different release times after the impulsive start of the flow: ○, release at $\tau = 29$; +, release at $\tau = 30$; □, release at $\tau = 32$, ×, release at $\tau = 33$.

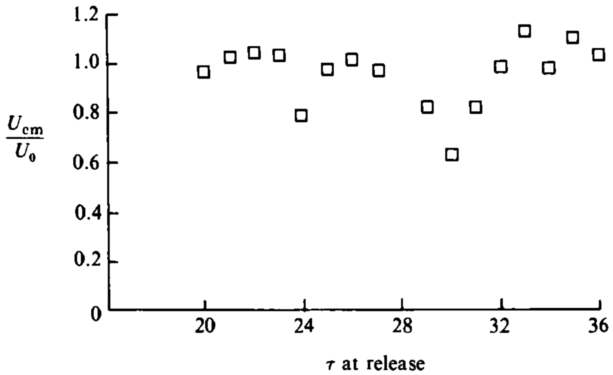

FIGURE 14. The computed speed of the centre of mass of the released fluid at time $\tau = 15$ after release in a flow with a well-developed wake at $Re = 484$ as a function of time of release.

problem (figure 7). The influence of the wake is apparent in the asymmetry of the released fluid. This is dependent upon the exact release time since the wake is oscillatory and the horseshoe shape may develop in a more or less symmetric manner. At some stage the speed of the centre of mass becomes greater than the onset flow velocity as released fluid is entrained by an area of vorticity which imposes a velocity in the downstream direction. In certain cases this holds at least until time $\tau = 15$ after release but this is unlikely to be maintained and the speed will presumably oscillate about the onset flow velocity until, after a very long time, the wake and released fluid become so diffuse that they travel downstream at the onset flow velocity.

The horseshoe shape is generally well formed by time $\tau = 5$ after release and the ends can appear to join up forming a roughly circular loop of fluid before breaking up. Figure 14 shows the speed of the centre of mass at time $\tau = 15$ after release as a function of the time of release. Remarkably, with release at $\tau = 30$, the initial horseshoe returns to a roughly circular area of enclosed fluid with a speed of $0.6U_0$. It is of course unlikely that this will be maintained and the result is not reproduced with fluid released in other half-cycles of vortex shedding. This emphasises the sensitivity of the motion of the released fluid to the structure of the wake at release. Comparing the inviscid-flow results shown in figure 8 with the present case, we see that the speed initially increases more rapidly in the former case, achieving a maximum speed of $0.8U_0$ at $\tau \approx 2$, but that the present case achieves a larger speed ($\approx U_0$) at $\tau \approx 5$. The ultimate speed is also likely to be greater than in the inviscid-flow case.

4. Experiments

The experiments we performed were rather simple in design and execution and were intended mainly for qualitative comparison with the numerical results described in the previous sections. We used the continuous-flow water channel described by Britter & Simpson (1978). The working section of this tank is 16.5 cm wide and about 1 m long. The available range for the mean speed U_0 of the flow in the channel is from 1 to 6 cm/s. An experiment was performed by placing a plastic tube of circular cross-section in the flow about 25 cm from the beginning of the working section, adding a small amount of coloured dye or fluorescein to the fluid inside the tube, and then withdrawing the tube vertically by hand. The resulting motion was photographed from directly above the release point with a motor-driven camera at an exposure rate of three frames per second.

It is not clear that the inviscid flow we have described can be produced in practice. After some trial and error attempts we were able to produce qualitatively similar results, although viscosity seemed to play a much stronger role than in the numerical computations. We used a shallow flow, about 1.6 cm deep, a flow speed of 1.8 cm/s (as measured by timing the movement of a small patch of dye on the surface), and a tube with a radius of 2.5 cm. This produced a flow with a small, nearly closed recirculation region just downstream of the cylinder. For this case we used dye to visualize the motion of the released fluid. Sequential photographs of the flow are shown in figure 15(*a*). The last photograph in the sequence corresponds roughly to $\tau = 2$ (or slightly less depending on how U_0 is defined in a flow where the upstream velocity profile is non-uniform). The photographs show a distinct roll-up of the released fluid into a pair of contrarotating vortices. However, the spirals are not as tight as in our numerical calculations. In fact, the loosely wound spirals appear like the vortex-blob calculations for a much larger core size than we used for the results in figure 6.

The wake problem was simulated by using a depth of 6 cm in the tank and flow speeds greater than 1 cm/s. These conditions produced a flow with a Kármán-vortex-street wake downstream of the cylinder. In this case we used fluorescein illuminated from the side by slit lighting to visualize the flow. The slit of light was about 1 cm wide and illuminated a horizontal slice of the channel about 1 cm below the free surface. Sequential photographs of the motion with $r_0 = 2$ cm and $U_0 = 4$ cm/s ($Re = 1600$) are shown in figure 15(*b*). These photographs were taken at 0.67 s intervals. The last photograph in the series corresponds to $\tau = 7$ in figure 12. The general shapes are roughly the same, although the experimental ones are more symmetric (but this is only a matter of timing). Other experiments showed markedly asymmetric behaviour. The contrast with figure 15(*a*) is very apparent. In the present case, the released fluid evolves into a thin, horseshoe shape, as opposed to a pair of diffuse contrarotating vortices. We performed experiments for Reynolds numbers in the range 400–2400 and observed little qualitative change in the evolving shape of the released fluid.

We attempted to measure the position of the centroid of the released fluid as a function of time after release in this latter series of experiments. The centroid at each

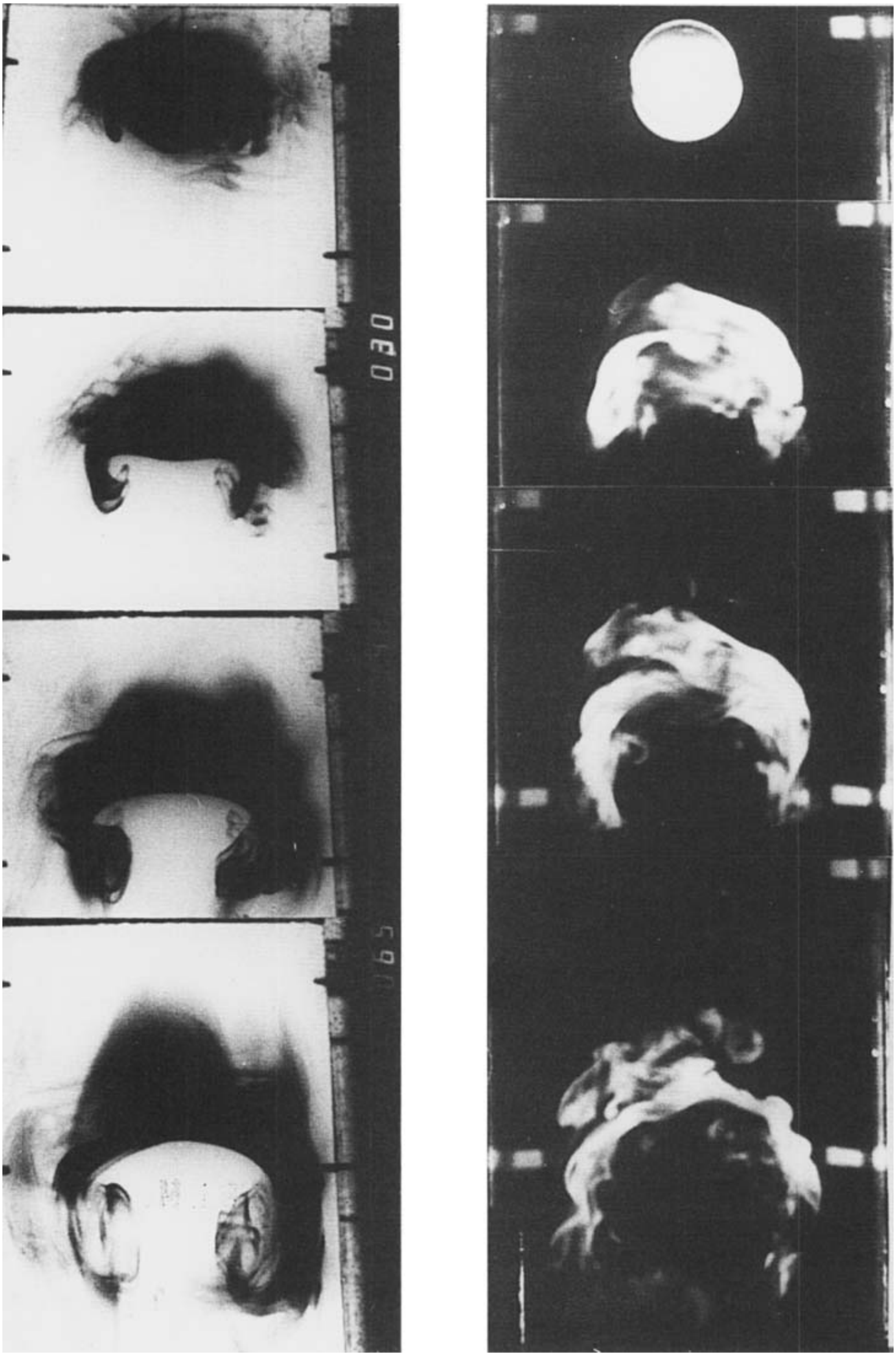

(a) (b)

FIGURE 15. Sequential photographs of the motion resulting from the release of a circular cylinder of dyed fluid in a uniform flow: (a) shallow flow simulating potential flow, $r_0 = 2.5$ cm, $U_0 = 1.8$ cm/s, $t = 1.33$ s, 1.67 s, 2.0 s, 2.33 s; (b) deep flow with $Re = 1600$, $r_0 = 2$ cm, $U_0 = 4$ cm/s, $t = 0$ s, 1.5 s, 3.2 s, 3.8 s.

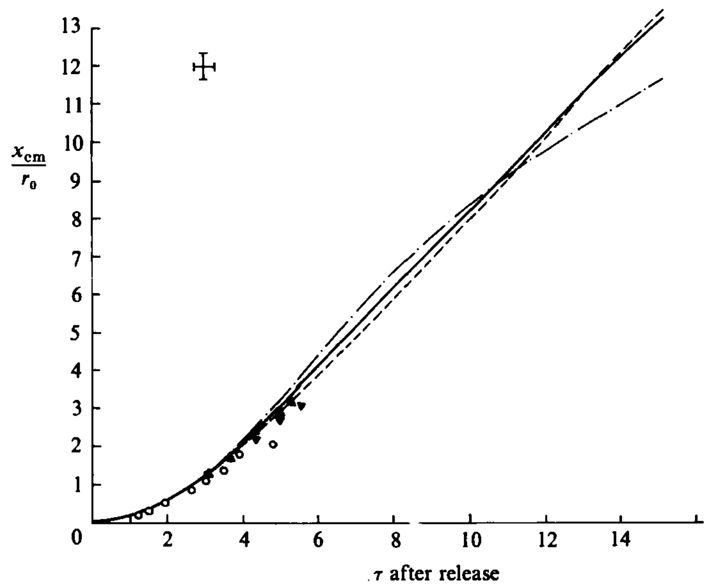

FIGURE 16. The computed position of the centre of mass of the fluid after release with a well-developed wake at $Re = 484$: —·—·—, release at $\tau = 30$; ——, release at $\tau = 32$; – – – –, release at $\tau = 33$. Experimental points are included for: ○, $Re = 440$; ▼, $Re = 800$; ▲, $Re = 1600$, with error bars in the top left-hand corner.

time interval was determined by projecting the photographic images onto cardboard, cutting out the image of the released fluid, and hanging this vertically from three different points. The intersection of three vertical lines drawn this way determines the geometric centroid within graphical accuracy. We also weighed the cardboard cutouts and found that the weight remained constant within 10% during an experiment, implying that the motion was roughly two-dimensional. With the geometric centroid of the released fluid known, its position relative to the release centre could be determined using reference markings in the photographs. This was a tedious process and therefore was only performed for three experimental runs. Although our measurements were subject to errors due to difficulties in determining the exact release time, the results of these three cases seemed fairly consistent. The experimental results and the computed results are plotted together in figure 16. The agreement is good although, with the uncertainties in determining the release times, this cannot be considered an entirely conclusive result.

Finally, we would like to compare our results qualitatively with the Thorney Island field trials. One difficulty with this comparison is that in most of the field trials a heavier-than-air gas (usually about twice the density of air) was released into a fairly light cross wind. This means that gravity played an important role, causing the released gas to collapse and spread out along the ground before the wind could have any significant effect. In a few of the early trials neutrally buoyant gas was released but unfortunately no photographs or measurements were taken. However, in one of the later trials (Trial 24) the conditions were such that part of the released gas was affected strongly by the wind and because of an accident in the set-up it is possible to see the motion of this part of the flow.

Figure 17 shows an overhead view of Trial 24 at about 4 s after the tent walls containing the gas were released. The tent is roughly circular in cross-section with

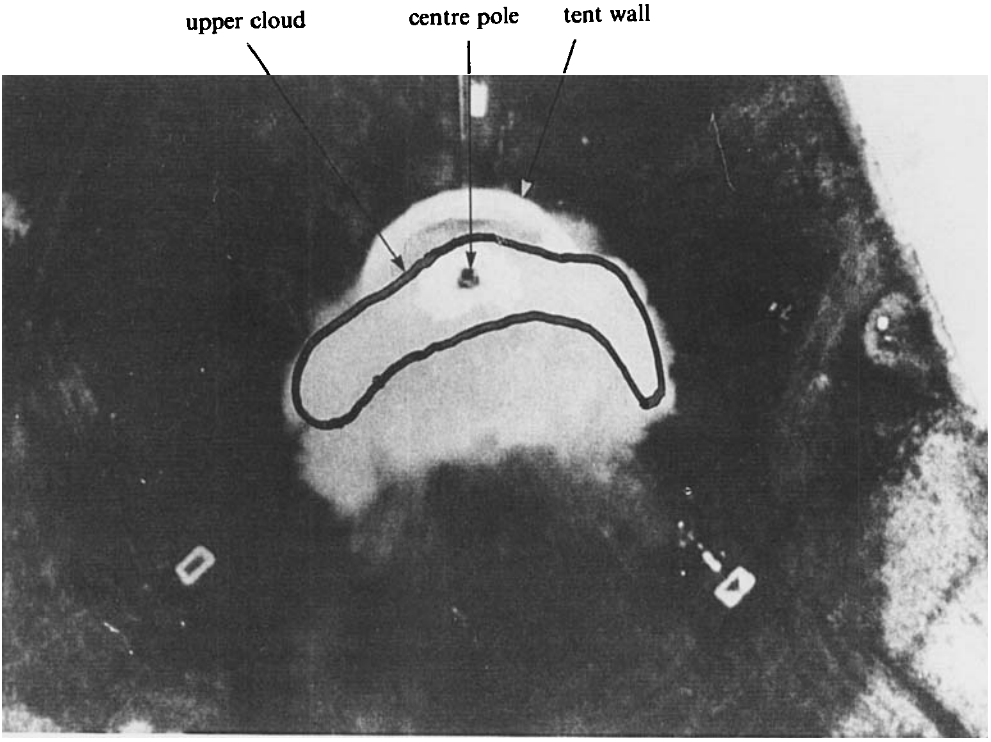

FIGURE 17. An overhead photograph of trial 24 of the Thorney Island field trials. The photograph was taken 4 s after the sides of the circular tent (visible in the photograph as a white circle) were pulled to the ground. The tent is 10 m in diameter and the wind is from the top of the photograph with a speed of about 7 m/s. The less dense section of the cloud has formed a crude horseshoe shape above the denser cloud that is spreading over the ground.

a diameter of 10 m and a height of 13 m. The cross wind speed in this particular trial was measured to be 7 m/s at 10 m above the ground. By accident in this trial only the top half of the tent was filled with the coloured smoke used to mark the fluid inside the tent. When the heavy gas collapses to the ground, mixing at the upper part of the cloud leaves a volume of gas that is much less dense than the rest of the cloud but is coloured by the smoke. This less dense cloud is swept downstream by the wind as we have described. In this particular case it is more easily visible from an overhead view since the main cloud, which is underneath the less dense cloud, contains less smoke than usual. This dilute smoke cloud shows all the major features we have described for the viscous-flow problem here, although the details of the two flows are different since the Reynolds number for this field trial is several orders of magnitude greater than our numerical calculations and the 'end' conditions are completely different.

The photograph shows that the cloud has expanded significantly in the direction perpendicular to the free-stream flow direction and that the upper cloud has deformed into a broad horseshoe shape. This photograph corresponds to a time $2 \leqslant \tau \leqslant 3$ (taking into account that the tent walls require about 2 s to be pulled to the ground). Considering all the differences in the two configurations and the difficulties in determining the exact release time, the correspondence with the computations in figure 12 is quite good.

5. Concluding remarks

We have applied a variety of numerical methods and a few analytical techniques in an attempt to determine the flow that results when a circular cylinder of fluid at rest is released into a cross-flow. Our results indicate that when the fluids are strictly inviscid a solution exists only for a very short time after the cylinder of fluid is released. The vortex sheet develops a singularity at some finite time, as has been found by earlier investigators working on related problems. Soon after the appearance of the singularity, the numerical methods become unstable.

One way to avoid this difficulty is to allow the vortex sheet to have a finite thickness. We used two numerical schemes that, in effect, give the vortex sheet a finite thickness in a somewhat *ad hoc* way. These methods may be thought of as producing 'weak' solutions, by analogy with shock solutions of hyperbolic problems. We have compared these calculations with cases where a thin layer of vorticity is produced in a viscous starting flow before release. The results of all three approaches differ mainly in their fine-scale structure; the larger features of the flow agree fairly well.

We have also considered the viscous problem when a wake is present before the cylinder of fluid is released. The general form of the released fluid, its deformation into a horseshoe shape, is basically similar to the inviscid case at early times, but the orientation and eventual speed of the released fluid is quite sensitive to when the release takes place during the wake's shedding cycle. Of course, the long-time behaviour, when viscosity has had sufficient time to thoroughly diffuse the vorticity in the flow, is quite different from the inviscid case.

Although we have performed these calculations and experiments for two specific and idealized problems, we hope our results may provide some insight into more fundamental problems. For example, mixing in fluids can be thought of in terms of blobs of fluid being injected or transported into different regions of a flow where velocity and perhaps density are different from where the blobs came. How these blobs accelerate and deform in their new environment determines mixing efficiency. Also, structures similar to those that we have computed have been seen making up the streaklines associated with turbulent boundary layers.

We would like to thank A. J. Roberts for help with adapting his vortex-sheet program to our problem, and J. M. R. Graham and J. C. R. Hunt for several informative discussions. The referees comments were most helpful in developing this work. J.W.R. was supported by the U.K. Health & Safety Executive under Contract 1918/01.01. The vortex-in-cell computations were made at the University of Manchester Regional Computer Centre.

Appendix A. The vortex-sheet method

The entire flow is determined by the position, shape and strength of the vortex sheet that marks the interface between the fluid that was originally inside the cylinder and that outside. Any distribution of vorticity on $S(t)$ describes a flow that satisfies (2.1)–(2.3). Since the vortex sheet is transported with the fluid, knowledge of the flow field determines the shape and position of $S(t)$. The boundary condition (2.4) determines the time evolution of the distribution of vorticity on $S(t)$.

The velocity field for a given distribution of vorticity on a surface in the fluid may be determined from the complex potential function $f(z)$:

$$f(z) = \frac{-\mathrm{i}}{2\pi}\oint \gamma \log\left[z-Z\right] \mathrm{d}\theta_0 + U_0 z, \tag{A 1}$$

where $z = x + \mathrm{i}y$ is the complex position of the field, $Z = Z(\theta_0, t) = X(\theta_0, t) + \mathrm{i}Y(\theta_0, t)$ is the complex position on the interface, $\gamma = \gamma(\theta_0, t)$ is the vorticity strength per unit θ_0, and θ_0 is a parameter that describes the interface (the initial angular position of the points on the interface). The velocity field everywhere except on the interface is given by

$$u - \mathrm{i}v = \frac{\mathrm{d}f}{\mathrm{d}z} = \frac{-\mathrm{i}}{2\pi}\oint \frac{\gamma\, \mathrm{d}\theta_0}{z - Z} + U_0. \tag{A 2}$$

As z approaches $Z' = Z(\theta_0', t)$ a point on the interface, from inside the contour or outside the contour, we find that

$$u - \mathrm{i}v \rightarrow U_{\mp} - \mathrm{i}V_{\mp} = -\frac{\mathrm{i}}{2\pi}\oint \frac{\gamma\, \mathrm{d}\theta_0}{Z' - Z} \mp \tfrac{1}{2}\gamma' \left(\frac{\partial Z}{\partial \theta_0}\right)^{-1}_{\theta_0 = \theta_0'} + U_0 \tag{A 3}$$

where the minus sign is chosen for inside the contour, the plus sign for outside the contour and $\gamma' = \gamma(\theta_0', t)$. The integral is a Cauchy principal value integral and the derivation of the above formula involves the use of the Plemelj formula.

The equations describing the position of the interface are

$$\frac{\mathrm{D}X}{\mathrm{D}t} = (1-\alpha)\, U_- + \alpha U_+; \tag{A 4}$$

$$\frac{\mathrm{D}Y}{\mathrm{D}t} = (1-\alpha)\, V_- + \alpha V_+, \tag{A 5}$$

where

$$\mathrm{D}/\mathrm{D}t \equiv \partial/\partial t + [(1-\alpha)\, \boldsymbol{U}_- + \alpha \boldsymbol{U}_+]\cdot\boldsymbol{\nabla}. \tag{A 6}$$

Since $\boldsymbol{U}_- \equiv (U_-, V_-)$ and $\boldsymbol{U}_+ \equiv (U_+, V_+)$ have equal components normal to the interface, α may be any function of θ_0 and t. We chose $\alpha = 0$ when $0 \leqslant \rho_2/\rho_1 \leqslant 1$ and $\alpha = 1$ when $\rho_2/\rho_1 \geqslant 1$ to avoid a numerical instability described by Roberts (1983).

Finally, the time evolution of γ is determined by solving the following pair of equations. From (2.8) and using (A 4)–(A 6) we obtain the first equation

$$\frac{\mathrm{D}\phi}{\mathrm{D}t} = \frac{1}{2}\left(\boldsymbol{U}_-^2 - 2\frac{\rho_2}{\rho_1}\boldsymbol{U}_-\cdot\boldsymbol{U}_+ + \frac{\rho_2}{\rho_1}\boldsymbol{U}_+^2\right) - \alpha\left[\boldsymbol{U}_-^2 - \left(1 + \frac{\rho_2}{\rho_1}\right)\boldsymbol{U}_-\cdot\boldsymbol{U}_+ + \frac{\rho_2}{\rho_1}\boldsymbol{U}_+^2\right], \tag{A 7}$$

where $\phi = \phi_1 - (\rho_2/\rho_1)\,\phi_2$. We obtain the second equation by differentiating (A 1) with respect to θ_0 and taking the real part,

$$\left.\frac{\partial \phi}{\partial \theta_0}\right|_{\theta_0 = \theta_0'} = -\frac{1}{2}\left(1 + \frac{\rho_2}{\rho_1}\right)\gamma' + \left(1 - \frac{\rho_2}{\rho_1}\right)\frac{1}{2\pi}\oint\left\{\gamma\ \mathrm{Im}\left[\frac{\partial Z/\partial\theta_0}{Z' - Z}\right]\right\}\mathrm{d}\theta_0 + \left(1 - \frac{\rho_2}{\rho_1}\right) U_0 \left.\frac{\partial X}{\partial \theta_0}\right|_{\theta_0 = \theta_0'}. \tag{A 8}$$

Thus, given Z and ϕ at some time, the evolution of the interface can be determined by evaluating (A 3)–(A 5) and solving (A 7) and (A 8).

We did this numerically using essentially the algorithm devised by Roberts (1983). This algorithm is particularly fast and accurate because it uses fast Fourier transforms to compute the derivatives and the trapezoidal rule for the integrals. Since we work with a closed interface, all functions are periodic in θ_0 and therefore the errors in these numerical methods are exponentially small. For further details of the method and its implementation, the reader is referred to Robert's paper. We note here that, since the flow is symmetric about the x-axis, we actually only computed the flow above the axis. However, in the text the number of points stated to describe the interface is the number of points on the whole interface, i.e. twice the number of points used in the calculation.

The inviscid problem has several integral invariants that are useful for monitoring the accuracy of the calculation. These, and their values for our problem, are

$$A = -\oint_{S(t)} y \frac{\mathrm{d}x}{\mathrm{d}\theta_0} \mathrm{d}\theta_0 = \pi r_0^2, \tag{A 9}$$

$$I_x = \rho_1 \oint_{S(t)} \left[\phi - \left(1 - \frac{\rho_2}{\rho_1}\right) U_0 x\right] \frac{\mathrm{d}y}{\mathrm{d}\theta_0} \mathrm{d}\theta_0 = -(\rho_1 + \rho_2) \pi U_0 r_0^2, \tag{A 10}$$

$$T = \tfrac{1}{2}\rho_1 \oint_{S(t)} \left[\phi - \left(1 - \frac{\rho_2}{\rho_1}\right) U_0 x\right] \left\{\left(\frac{\partial \phi_1}{\partial x} - U_0\right) \frac{\mathrm{d}y}{\mathrm{d}\theta_0} - \frac{\partial \phi}{\partial y} \frac{\mathrm{d}x}{\mathrm{d}\theta_0}\right\} \mathrm{d}\theta_0 = \tfrac{1}{2}(\rho_1 + \rho_2) \pi U_0^2 r_0^2, \tag{A 11}$$

where A is the area of the released fluid, I_x is the horizontal component of the fluid impulse and T is the kinetic energy of the flow in a reference frame in which the fluid speed at infinity is zero. These quantities are derived, for example, in Batchelor (1967, pp. 527–530) and the above formulae for them are obtained by judicious use of Green's theorem.

Two other quantities used in the presentation of results are the curvature

$$\xi = \left(\frac{\mathrm{d}X}{\mathrm{d}\theta_0} \frac{\mathrm{d}^2 Y}{\mathrm{d}\theta_0^2} - \frac{\mathrm{d}Y}{\mathrm{d}\theta_0} \frac{\mathrm{d}^2 X}{\mathrm{d}\theta_0^2}\right) \Big/ \left[\left(\frac{\mathrm{d}X}{\mathrm{d}\theta_0}\right)^2 + \left(\frac{\mathrm{d}Y}{\mathrm{d}\theta_0}\right)^2\right]^{\frac{3}{2}} \tag{A 12}$$

and the so-called true vorticity strength (the vorticity strength per unit arc length)

$$\omega = \gamma \Big/ \left[\left(\frac{\mathrm{d}X}{\mathrm{d}\theta_0}\right)^2 + \left(\frac{\mathrm{d}Y}{\mathrm{d}\theta_0}\right)^2\right]^{\frac{1}{2}}. \tag{A 13}$$

Appendix B. The vortex-blob method

The vortex-blob method, which was introduced by Chorin & Bernard (1973), for desingularizing the evolution of vortex sheets has a variety of different implementations. Many of these are reviewed by Leonard (1980). The particular implementation we chose, mainly because it was the easiest modification of our vortex-sheet formulation, is that due to Krasny (1986*b*). The modification, which only applies when $\rho_2/\rho_1 = 1$, consists of replacing (A 4) and (A 5) with

$$\frac{\mathrm{D}X}{\mathrm{D}t} = -\frac{1}{2\pi} \oint \frac{\gamma(Y' - Y)\,\mathrm{d}\theta_0}{[(X' - X)^2 + (Y' - Y)^2 + \delta^2]} + U_0, \tag{B 1}$$

$$\frac{\mathrm{D}Y}{\mathrm{D}t} = \frac{1}{2\pi} \oint \frac{\gamma(X' - X)\,\mathrm{d}\theta_0}{[(X' - X)^2 + (Y' - Y)^2 + \delta^2]}, \tag{B 2}$$

and (A 7) and (A 8) with

$$\frac{\mathrm{D}\phi}{\mathrm{D}t} = 0, \tag{B 3}$$

$$\left.\frac{\partial \phi}{\partial \theta_0}\right|_{\theta_0 = \theta_0'} = -\gamma', \tag{B 4}$$

where δ is a positive real number (a measure of the core size). When $\delta = 0$, (B 1)–(B 4) are the same as (A 4)–(A 8) with $\rho_2/\rho_1 = 1$ and $\alpha = \frac{1}{2}$. When $\delta > 0$, the integrals in (B 1) and (B 2) are proper and for small δ are a desingularized approximation of the exact vortex-sheet evolution equations. Typically in the calculations for the present paper $\delta \approx 0.1 r_0$.

Appendix C. The random walk/vortex-in-cell method

In two dimensions the flow around cylindrical bodies may be described by the vorticity equation

$$\frac{\mathrm{D}\omega}{\mathrm{D}t} = \nu \nabla^2 \omega, \tag{C 1}$$

with specified onset flow conditions and zero-slip and zero-normal-velocity conditions imposed at solid surfaces. In (C 1) ω is vorticity ($\omega = \nabla \times \boldsymbol{u}$) and ν is kinematic viscosity. Vorticity is related to stream function ψ through the Poisson's equation

$$\nabla^2 \psi = -\omega, \tag{C 2}$$

and ψ is related to velocity by

$$\boldsymbol{u} = \nabla \psi \times \boldsymbol{k}, \tag{C 3}$$

where $\boldsymbol{k}$ is a unit vector perpendicular to the plane of the flow.

Using Chorin's (1973) fractional-step method to advance vorticity in time, the inviscid part of the vorticity equation is solved by time-stepping discrete vortices and the diffusive part is added by superimposing normally distributed random walks on the orthogonal coordinates of each vortex at each time-step. The variance of the random walk has a magnitude of $2\nu\Delta t$ where Δt is the time-step. One attraction of the method is that it avoids numerical diffusion problems associated with Eulerian schemes. The method has been widely tested with idealized and applied problems which will not be reviewed here.

In this application, which closely follows Stansby & Dixon (1983), the zero-velocity condition at a surface is satisfied at each time-step by introducing a vortex sheet through a standard boundary-integral method. The sheet strength at equispaced points around the surface is determined from tangential velocities on the surface (in fact just inside the surface owing to numerical constraints) and an inverted influence matrix. The net circulation on the sheet is maintained at zero to ensure closure of the pressure integration as described below. The sheet is converted into discrete vortices for the numerical development. Vortices which random walk inside the surface are reflected on to their mirror-image positions outside to correctly maintain the tangential velocity condition on the surface (Chorin 1978).

The inviscid interaction of fields of vorticity may be calculated by the vortex-blob method which is a formally convergent solution when a blob core overlaps several adjacent blob centres (Hald 1979). This is roughly equivalent to there being several vortices per cell in the vortex-in-cell method which will now be described.

The principle of the method has been outlined in §2.4. The implementation used here is the same as that used by Stansby & Dixon (1983). Poisson's equation, (C 2), is solved using three rectangular overlapping meshes with uniform grid spacing. This is suited to the high-Reynolds-number wake problem where a fine inner mesh provides definition in the boundary layer, an intermediate mesh allows rolling-up in the near-wake region and a coarse outer mesh transports large structures downstream.

The meshes are solved sequentially from the coarse outer mesh inwards. The boundary of the outer mesh is sufficiently far from the vorticity (which has zero net circulation) for the stream function on the outer boundary due to vorticity to be set to zero. To solve on the intermediate mesh the stream function on its boundary is obtained from the coarse-mesh solution and to solve on the fine mesh the stream function on its boundary is obtained from the intermediate-mesh solution. For these applications cell sizes of 0.04, 0.16 and 0.64 cylinder radii were used with 64×64, 64×40 and 128×40 meshes respectively. The inner-cell size is close to the standard deviation of the random walk with $Re = 484$. The velocity at a point is calculated from the mesh with the smallest possible cell size. After release of the cylinder of fluid the vortex positions are adjusted so that the centre of mass of the released fluid is also the centre of the inner mesh so that the development of the main region of interest has the best definition available.

The surface vortex sheet is divided into 60 segments for the numerical calculation and each segment is then represented as one or more discrete vortices. The time-step $\Delta\tau$ was generally set to 0.1 although smaller values were used for checking.

To release the fluid within the cylinder the introduction of the vortex sheet at the surface is simply stopped. The interface between the interior and exterior fluids quickly becomes ill-defined, owing to diffusion in the viscous case and to fine-scale grid-dependent behaviour in the inviscid case. To compute the motion of the interior fluid it is represented by a uniform distribution of markers with initial spacings of 0.04 radii in the x- and y-directions. Once the fluid is released, the positions of these markers are advanced in time in the same way that the discrete vortices are advanced in time. There are thus 1963 markers in the flow and these are used to determine the position and speed of the centre of mass. In addition, since each marker may be considered to represent a small finite area of fluid they may be used to determine concentrations on a suitable mesh; for convenience we use the intermediate vortex-in-cell mesh. The area associated with each marker is converted into concentrations at mesh points using the same distribution procedure that is used to determine vorticity from the circulations of the discrete vortices (sometimes referred to as area weighting). There are sufficient fluid markers to produce smoothly varying concentrations and hence reasonable contour plots using a standard computer-graphics routine.

We finally describe an improved scheme for calculating the surface pressure distribution on a cylinder surface. At the wall the boundary-layer equation reduces to

$$\frac{1}{\rho}\frac{\partial p}{\partial s} = -\nu\frac{\partial \omega}{\partial n}, \tag{C 4}$$

where s is distance along the wall in a clockwise direction and n is distance normal to the wall. Also, the vorticity equation reduces to

$$\frac{\partial \omega}{\partial t} = \nu\frac{\partial^2 \omega}{\partial n^2}, \tag{C 5}$$

giving a circulation flux through the wall of $-\nu\partial\omega/\partial n|_{n=0}$ per unit length, and $-\nu\Delta t\,\partial\omega/\partial n|_{n=0}$ is thus the vortex sheet strength γ that is created on the surface in one time-step. The equation for pressure becomes

$$p = \rho\int\frac{\gamma}{\Delta t}\,\mathrm{d}s + p_0, \tag{C 6}$$

where p_0 is pressure at $s = 0$. For pressure to return to its original value once a circuit has been completed we require $\oint \gamma \, \mathrm{d}s = 0$ and this condition is included explicitly in the boundary-integral solution for γ.

REFERENCES

Baker, G. R. 1979 The cloud-in-cell technique applied to the roll-up of vortex sheets. *J. Comp. Phys.* **31**, 76–95.

Baker, G. R. 1980 A test of the method of Fink and Soh for following vortex-sheet motion. *J. Fluid Mech.* **100**, 209–220.

Batchelor, G. K. 1967 *An Introduction to Fluid Dynamics*. Cambridge University Press.

Britter, R. E. & Simpson, J. E. 1978 Experiments on the dynamics of a gravity current head. *J. Fluid Mech.* **88**, 223–240.

Chorin, A. J. 1973 Numerical study of slightly viscous flow. *J. Fluid Mech.* **57**, 785–796.

Chorin, A. J. 1978 Vortex sheet approximation of boundary layers. *J. Comp. Phys.* **27**, 428–442.

Chorin, A. J. & Bernard, P. S. 1973 Discretisation of a vortex sheet with an example of roll-up. *J. Comp. Phys.* **13**, 423–429.

Christiansen, J. P. 1973 Numerical simulation of hydrodynamics by a method of point vortices. *J. Comp. Phys.* **13**, 363–379.

Fink, P. T. & Soh, W. K. 1978 A new approach to roll-up calculations of vortex sheets. *Proc. R. Soc. Lond.* A **362**, 195–209.

Hald, O. 1979 The convergence of vortex methods II. *SIAM J. Numer. Anal.* **16**, 726–755.

Hall, D. J., Hollis, E. J. & Ishaq, H. 1984 A wind tunnel model of the Porton dense gas spill field trials. In *Proc. IUTAM Symp. on Atmospheric Dispersion of Heavy Gases and Small Particles, Delft, The Netherlands, August 1983* (ed. G. Ooms & H. Tennekes). Springer.

Krasny, R. 1986*a* A study of singularity formation in a vortex sheet by the point-vortex approximation. *J. Fluid Mech.* **167**, 65–93.

Krasny, R. 1986*b* Desingularization of periodic vortex sheet roll-up. *J. Comp. Phys.* **65**, 292–313.

Leonard, A. 1980 Vortex methods for flow simulation. *J. Comp. Phys.* **37**, 289–335.

McQuaid, J. 1984 Large scale experiments on the dispersion of heavy gas clouds. In *Proc. IUTAM Symp. on Atmospheric Dispersion of Heavy Gases and Small Particles, Delft, The Netherlands, August 1983* (ed. G. Ooms & H. Tennekes). Springer.

Meiron, D. I., Baker, G. R. & Orszag, S. A. 1982 Analytic structure of vortex sheet dynamics. Part I. Kelvin–Helmholtz instability. *J. Fluid Mech.* **114**, 283–298.

Moore, D. W. 1979 The spontaneous appearance of a singularity in the shape of an evolving vortex sheet. *Proc. R. Soc. Lond.* A **365**, 105–119.

Moore, D. W. 1981 On the point vortex method. *SIAM J. Sci. Stat. Comput.* **2**, 65–84.

Picknett, R. G. 1981 Dispersion of dense gas puffs released in the atmosphere at ground level. *Atmos. Environ.* **15**, 509–525.

Pierrehumbert, R. T. 1980 A family of steady, translating vortex pairs with distributed vorticity. *J. Fluid Mech.* **99**, 129–144.

Roberts, A. J. 1983 A stable and accurate numerical method to calculate the motion of a sharp interface between fluids. *IMA J. Appl. Maths.* **31**, 13–35.

Saffman, P. G. & Baker, G. R. 1979 Vortex interactions. *Ann. Rev. Fluid Mech.* **11**, 95–112.

Schwartz, L. W. 1981 A semi-analytic approach to self-induced motion of vortex sheets. *J. Fluid Mech.* **111**, 475–490.

Smith, P. A. 1986 Computation of viscous flows by the vortex method. PhD thesis, University of Manchester.

Smith, P. A. & Stansby, P. K. 1985 Wave-induced bed flows by a Lagrangian vortex scheme. *J. Comp. Phys.* **60**, 489–516.

STANSBY, P. K. & DIXON, A. G. 1983 Simulation of flows around cylinders by a Lagrangian vortex scheme. *Appl. Ocean. Res.* **5**, 167–178.

TAYLOR, G. I. 1953 Formation of a vortex ring by giving an impulse to a circular disc and the dissolving it away. *J. Appl. Phys.* **24**, 104–105.

THOM, A. 1928 An investigation of fluid flow in two dimensions. *Aero. Res. Counc. R & M*, No. 1194, 166–183.